Chemical Science

ROYAL SOCIETY OF CHEMISTRY

EDGE ARTICLE

View Article Online
View Journal | View Issue

Cite this: *Chem. Sci.*, 2021, **12**, 730

All publication charges for this article have been paid for by the Royal Society of Chemistry

Holmium(III) molecular nanomagnets for optical thermometry exploring the luminescence re-absorption effect†

Junhao Wang, [a] Jakub J. Zakrzewski, [b] Mikolaj Zychowicz, [bc] Veacheslav Vieru, [cd] Liviu F. Chibotaru, [c] Koji Nakabayashi, [a] Szymon Chorazy *[b] and Shin-ichi Ohkoshi *[a]

Coordination complexes of lanthanide(3+) ions can combine Single-Molecule Magnetism (SMM) with thermally modulated luminescence applicable in optical thermometry. We report an innovative approach towards high performance SMM-based optical thermometers which explores tunable anisotropy and the luminescence re-absorption effect of Ho^{III} complexes. Our concept is shown in dinuclear cyanido-bridged molecules, $\{[Ho^{III}(4\text{-pyridone})_4(H_2O)_2][M^{III}(CN)_6]\}\cdot nH_2O$ (M = Co, **1**; Rh, **2**; Ir, **3**) and their magnetically diluted analogues, $\{[Ho^{III}{}_xY^{III}{}_{1-x}(4\text{-pyridone})_4(H_2O)_2][M^{III}(CN)_6]\}\cdot nH_2O$ (M = Co, $x = 0.11$, **1@Y**; Rh, $x = 0.12$, **2@Y**; Ir, $x = 0.10$, **3@Y**). They are built of pentagonal bipyramidal Ho^{III} complexes revealing the zero-dc-field SMM effect. Experimental studies and the *ab initio* calculations indicate an Orbach magnetic relaxation with energy barriers varying from 89.8 to 86.7 and 78.7 cm^{-1} K for **1**, **2**, and **3**, respectively. **1–3** also differ in the strength of quantum tunnelling of magnetization which is suppressed by hyperfine interactions, and, further, by the magnetic dilution. The Y^{III}-based dilution governs the optical properties as **1–3** exhibit poor emission due to the dominant re-absorption from Ho^{III} while **1@Y–3@Y** show room-temperature blue emission of 4-pyridone. Within ligand emission bands, the sharp re-absorption lines of the Ho^{III} electronic transitions were observed. Their strong thermal variation was used in achieving highly sensitive ratiometric optical thermometers whose good performance ranges, lying between 25 and 205 K, are adjustable by using hexacyanidometallates. This work shows that Ho^{III} complexes are great prerequisites for advanced opto-magnetic systems linking slow magnetic relaxation with unique optical thermometry exploiting a luminescence re-absorption phenomenon.

Received 3rd September 2020
Accepted 30th October 2020

DOI: 10.1039/d0sc04871b

rsc.li/chemical-science

Introduction

Broad scientific interest is currently devoted to advanced opto-magnetic materials combining magnetic properties, including ferromagnetism or spin transitions, with optical functionalities such as photo-induced phase transitions or luminescence.[1–8] Among modern magnetic materials, Single-Molecule Magnets (SMMs) stand at the research forefront as they reveal a slow magnetic relaxation effect resulting in the hysteresis loop of a molecular origin.[9,10] It opens applications in high-density information storage,[11,12] spintronics,[13] and quantum computing.[14] In the pursuit towards novel opto-magnetic systems, lanthanide(III) SMMs are of primary interest due to the designable conjunction of magnetic anisotropy and luminescence related to their f–f electronic transitions.[15,16] They exhibit the highest anisotropic energy barriers producing the magnetic bistability even at 80 K,[17,18] and form a unique class of luminescent SMMs showing magneto–optical correlations,[19–27] and the perspective for magnetic switching of emission.[28]

Recently, a research pathway consisting of the application of lanthanide SMMs in the construction of luminescent molecular thermometers emerged.[29–34] Optical thermometry utilizing thermally activated luminescence of f-block metal ions was broadly investigated in the last decade[35–39] as it opens the avenue to contactless temperature sensors for electronic

[a]*Department of Chemistry, School of Science, The University of Tokyo, 7-3-1 Hongo, Bunkyo-ku, Tokyo 113-0033, Japan. E-mail: ohkoshi@chem.s.u-tokyo.ac.jp*

[b]*Faculty of Chemistry, Jagiellonian University, Gronostajowa 2, 30-387 Kraków, Poland. E-mail: chorazy@chemia.uj.edu.pl*

[c]*Theory of Nanomaterials Group, Katholieke Universiteit Leuven, Celestijnenlaan 200F, 3001 Leuven, Belgium*

[d]*Maastricht Science Programme, Faculty of Science and Engineering, Maastricht University, Paul-Henri Spaaklaan 1, 6229 EN Maastricht, The Netherlands*

† Electronic supplementary information (ESI) available: Experimental details. IR spectra. TGA curves. Detailed structure parameters. Additional structural views. Results of continuous shape measure analysis. P-XRD patterns. Direct-current (dc) magnetic properties. Complete alternate-current (ac) magnetic characteristics. Details of *ab initio* calculations. Detailed discussion on the impact of hyperfine interactions on the electronic structure of Ho^{III} complexes. Solid-state UV-vis-NIR absorption spectra. Complete results of temperature-variable photoluminescent studies. CCDC 1983881–1983883. For ESI and crystallographic data in CIF or other electronic format see DOI: 10.1039/d0sc04871b

devices,[40] medical diagnostics,[41] or chemical reactors.[42] The molecular approach is particularly attractive due to the sensing ability at the nanoscale.[40–43] When combining this property with the SMM effect, multifunctional magnetic luminescent thermometers are accessible.[29–34] They can realize a multitasking concept,[33,44] and they are promising building blocks for smart electromagnetic SMM-based devices with a self-monitored temperature.[29]

Achieving optical thermometers using lanthanide SMMs demands the simultaneous design of magnetic anisotropy and thermally modulated emission. This challenging task was realized by applying intrinsic properties of Dy^{III} or Yb^{III} complexes.[29–34] The Dy^{III} centres reveal very strong magnetic anisotropy,[45] but their yellow luminescence is relatively weak, hampering the utility for optical thermometry.[46,47] Interest was also devoted to Yb^{III} due to its efficiently modulated NIR emission.[48–50] However, its magnetic relaxation has to be induced by a direct-current (dc) magnetic field due to the strong quantum tunnelling of magnetization (QTM).[51,52] These indicated a large difficulty in controlling of lanthanide anisotropy along with *T*-activated luminescence.

In this context, we propose the application of Ho^{3+} ions for high-performance SMM-based optical thermometers. The Ho^{III} centres are rarely used for SMMs but they can reveal the zero-dc-field slow magnetic relaxation in the axial distribution of charged ligands with the support of hyperfine interactions that suppress the QTM.[53–64] The classical luminescence from the Ho^{III} f–f electronic transitions is weak,[65,66] and an alternative up-conversion luminescence requires the presence of other 4f metal ions.[67] In contrast, Ho^{3+} ions exhibit an efficient luminescent re-absorption effect due to the numerous absorption peaks in the visible range.[68,69] Due to the presence of hot bands and variable thermal dependence of electronic transitions, the Ho^{III} absorption peaks can be strongly *T*-dependent,[70,71] which is a tool for optical thermometry.[72,73] Using the re-absorption effect, these absorption peaks may be easily detected on the emission pattern of the attached luminophore.[68,69] Following these perspectives, we decided to examine the idea of a Ho^{III}-SMM-based optical thermometer. We focused on lanthanide(III)–hexacyanidometallate(III) systems as cyanido transition metal complexes are efficient in inducing of both strong lanthanide magnetic anisotropy and tunable emission properties.[74–79] We selected the 4-pyridone ligands which exhibit pronounced blue emission and ensure substantial magnetic anisotropy of Dy^{III}.[79] Thus, we combined 4-pyridone with Ho^{III} and hexacyanidometallates of Co^{III}, Rh^{III}, and Ir^{III}, used to amend the properties of attached 4f-metal ions. We report structural, magnetic, and optical properties of the series of dinuclear molecules, $\{[Ho^{III}(4\text{-pyridone})_4(H_2O)_2][M^{III}(CN)_6]\}\cdot nH_2O$ (M = Co, **1**; Rh, **2**; Ir, **3**) and their magnetically diluted analogues, $\{[Ho_xY_{1-x}(4\text{-pyridone})_4(H_2O)_2][M(CN)_6]\}\cdot nH_2O$ (M = Co, $x = 0.11$, **1@Y**; Rh, $x = 0.12$, **2@Y**; Ir, $x = 0.10$, **3@Y**), showing the SMM effect and optical thermometry related to the Ho^{III} re-absorption effect within the 4-pyridone emission, with both effects modulated by $[M^{III}(CN)_6]^{3-}$ ions.

Results and discussion

Structural studies

After mixing of the hot aqueous solution containing Ho^{3+} ions and 4-pyridone with the cold aqueous solution of $[M^{III}(CN)_6]^{3-}$ (M = Co, Rh, and Ir) ions, yellowish block crystals of **1–3** were formed (see Experimental details in the ESI,†). After preliminary characterization through IR spectroscopy, TGA, and elemental analyses (Fig. S1–S2, Table S1†), the crystal structures of **1–3** were determined by using a single-crystal X-ray diffraction (SC-XRD) method (Table S2†). The structural analysis revealed that **1–3** are isostructural and consist of dinuclear $\{Ho^{III}[M^{III}(CN)_6]\}$ molecules crystallizing together with water of crystallization in the orthorhombic *Cmcm* space group (Fig. 1a, S3, and S4, and Table S3†). Each molecule is built of octahedral $[M^{III}(CN)_6]^{3-}$ ions bridged by a single cyanido ligand (C1–N1) to the Ho^{III} centre coordinating also four O-atoms of the 4-pyridone ligands and two O-atoms of water molecules. The resulting seven-coordinated Ho^{III} complexes resemble a four-blade propeller shape due to the specific alignment of 4-pyridone ligands within the ac plane (Fig. S4†) but, taking into account only atoms coordinated to Ho^{III}, its coordination geometry can be described as a distorted pentagonal bipyramid of the pseudo-D_{5h} symmetry (Fig. 1b, Table S4†). The axial positions are occupied by the O2 atoms of 4-pyridone ligands, and the O2–Ho1–O2 direction approximately corresponds to the easy magnetic axis of the complex (see below). The deviation from the strict D_{5h} symmetry is represented by the imperfect axiality depicted by the O2–Ho1–O2 angles of 167.4°, 169.7°, and 168.4° for **1**, **2**, and **3**, respectively, as well as by the non-ideal positions of O1, O3 and N1 atoms within the equatorial plane of the bipyramid (Fig. 1b and Table S3†). The cyanido-bridged molecules in **1–3** are stabilized in the respective supramolecular frameworks by the π–π stacking between aromatic groups of 4-pyridone ligands as well as the hydrogen bonding network involving terminal cyanides and water molecules. It makes the crystalline samples of **1–3** stable in air as proven by the powder

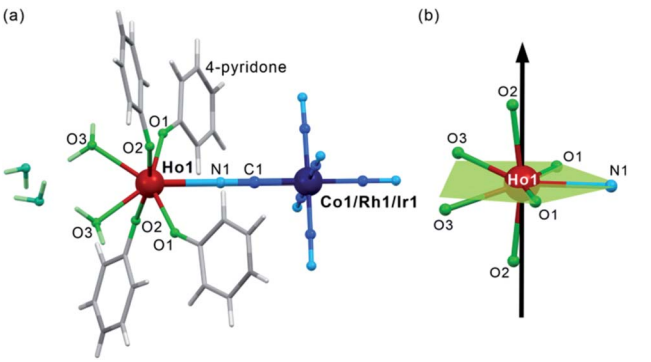

Fig. 1 The crystal structure of **1–3** presented using the structural model of **1**: the representative view of $\{Ho^{III}[M^{III}(CN)_6]\}$ (M = Co, Rh, Ir) molecules with accompanying crystallization water (a), and the insight into the Ho^{III} complexes with the indication of the equatorial plane of the pentagonal bipyramidal geometry (green) and the direction of their easy magnetic axis determined by the *ab initio* calculations (black arrow) (b).

X-ray diffraction (P-XRD) method confirming also the validity of the structural model for the bulk samples and their phase purity (Fig. S5†). For the studies of magnetic and optical properties, the Y^{III}-diluted samples of **1**, **2**, and **3**, named **1@Y**, **2@Y**, **3@Y**, respectively, were prepared and characterized (see Experimental details). They are isostructural with **1–3** as shown by the P-XRD patterns (Fig. S5†), thus, they consist of the identical $\{Ho^{III}[M^{III}(CN)_6]\}$ molecules dispersed in small amounts, 11%, 12%, and 10% for **1@Y**, **2@Y**, and **3@Y**, respectively, within the supramolecular matrix composed of the analogous $\{Y^{III}[M^{III}(CN)_6]\}$ units. We also prepared bimetallic Y^{III}–Co^{III} analogue (**4**), and the whole series of trimetallic $\{Ho_xY_{1-x}[Co^{III}(CN)_6]\}$ (x = 0.03, 0.05, 0.08, 0.16, 0.22, 0.33; **1@Y-Ho$_x$Y$_{1-x}$Co**) molecules, also isostructural to **1–3** (Fig. S6†).

Magnetic properties

Due to the presence of Ho^{III} complexes of the pseudo-D_{5h} geometry, which is a promising tool for the SMM effect,[61,63] magnetic properties of **1–3**, including direct-current (dc) and alternate-current (ac) magnetic measurements were investigated (Fig. 2, S7–S10, and Table 1). The room-temperature $\chi_M T$ values are 13.8, 13.7, and 13.7 cm^3 mol^{-1} K, for **1**, **2**, and **3**, respectively, which are close to the theoretical limit of 14.1 cm^3 mol^{-1} K for a free Ho^{3+} ion. The temperature dependences of the $\chi_M T$ for **1–3** reveal the monotonous decrease of the signal on cooling to *ca.* 12 cm^3 mol^{-1} K at T = 2 K which is due to the gradual depopulation of the m_J states within the ground $^5I_8$ multiplet (Fig. S7†). No drastic changes in the $\chi_M T(T)$ plots was observed indicating a lack of significant magnetic coupling as expected for Ho^{III} centres separated by diamagnetic 4-pyridone ligands and $[M^{III}(CN)_6]^{3-}$ ions. Field dependences of magnetization at T = 2 K also show a featureless increase with increasing field to 5.0 μ_B at 50 kOe, which lies in the range typical for uncoupled Ho^{III} centres (Fig. S7,† the insets).[53–64]

The ac magnetic characteristics gathered with an oscillating ac field of 3 Oe indicate the presence of zero-dc-field slow magnetic relaxation in **1–3** (Fig. 2, and S8–S10†). In the frequency range of 0.5–1500 Hz, the non-negligible ac signal was found from 2 K to 17 K (Fig. S8–S10†), however, the $\chi'_M(\nu)$ and $\chi''_M(\nu)$ dependences could be analysed using a generalized Debye model for the T-range of 2–14 K (Fig. 2a). The model employing a single relaxation process was used, however, the frequency ranges were limited as the visible tails in the $\chi''_M(\nu)$ plots were observed. This can be ascribed to the disturbing influence of dipolar interactions between neighbouring Ho^{III} centres insufficiently isolated within the structures of **1–3**.[76,80] To prove this, the magnetically diluted analogues, **1@Y–3@Y** were also examined (Fig. 2a, and S11–S20, Table S5†). They

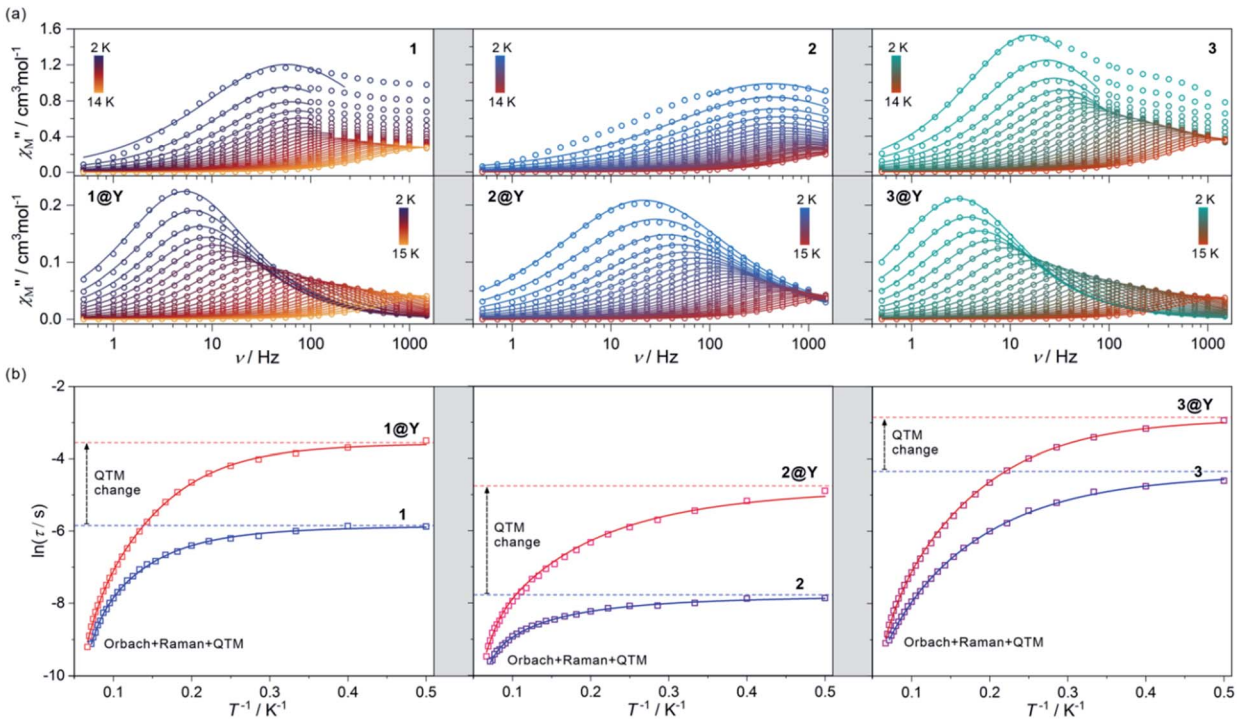

Fig. 2 The alternate-current (ac) magnetic characteristics of **1** (left), **2** (centre), and **3** (right), and their respective magnetically diluted samples, **1@Y** (left), **2@Y** (centre), and **3@Y** (right): the frequency dependences of the out-of-phase magnetic susceptibility, $\chi''_M(\nu)$, at H_{ac} = 3 Oe and H_{dc} = 0 Oe in the indicated temperature ranges with the fittings according to the generalized Debye model (a), the temperature dependences of the resulting relaxation times, shown in the form of $\ln(\tau) = f(T^{-1})$, fitted using the combined contributions from Orbach, Raman and QTM processes (b) (see Table 1 for the best-fit parameters). The empty circle (a) and square (b) points represent the experimental data while the solid lines represent the respective fits. In (b), the additional dashed lines represent the fitted contributions from the QTM effect. The fitting of zero-dc-field magnetic data was performed for **1–3** while the simultaneous fitting of magnetic relaxation times both for zero and optimal dc fields was performed for **1@Y–3@Y** (see Fig. S11–S20, Table S5† and text for details).

Table 1 Best-fit parameters for contributions from Orbach, Raman, and QTM effects to the overall magnetic relaxation fitted using eqn (1) to the experimental temperature dependences of relaxation time in **1**, **2**, and **3**, and their magnetically diluted samples, **1@Y**, **2@Y**, and **3@Y** (Fig. 1 and S8–S20), and the respective best-fit parameters for the linear fitting of the higher temperature range of the $\ln(\tau)-T^{-1}$ plots, obeying the Arrhenius law (eqn (1) limited to the Orbach contribution). The values of energy barriers of the Orbach relaxation were taken from the results of *ab initio* calculations (Fig. 3) and fixed during the fitting procedure. The detailed results of the simultaneous fitting of the temperature dependences of relaxation times under zero and optimal dc fields in **1@Y–3@Y**, together with the alternative fitting with the free ΔE value, are discussed in the ESI (Fig. S20, Table S5)

Fitting type	Parameter	1	1@Y	2	2@Y	3	3@Y
Overall fitting with Orbach, Raman and QTM relaxation processes	ΔE in cm^{-1}	89.8 cm^{-1}		86.7 cm^{-1}		78.7 cm^{-1}	
	[$\Delta E/k_B$ in K] (fixed)	[129.2 K]		[124.8 K]		[113.2 K]	
	τ_0/s	$3.3(4) \times 10^{-8}$	$6.0(6) \times 10^{-8}$	$4.0(6) \times 10^{-8}$	$5.5(6) \times 10^{-8}$	$4.8(2) \times 10^{-6}$	$2.3(3) \times 10^{-7}$
	C_{Raman}/s^{-1} K^{-n}	1.9(3)	0.12(2)	64(13)	6.6(8)	2.2(2)	0.20(2)
	n	3.04(8)	3.95(5)	1.90(8)	2.57(5)	3.09(3)	3.77(4)
	τ_{QTM}/s	0.00289(7)	0.0286(9)	0.00042(13)	0.0086(6)	0.0130(4)	0.058(3)
Limited fitting according to the Arrhenius law	ΔE in cm^{-1}	40(2) cm^{-1}	87(3) cm^{-1}	25(4) cm^{-1}	78(4) cm^{-1}	31.3(9) cm^{-1}	73.0(14) cm^{-1}
	[$\Delta E/k_B$ in K]	[57(3) K]	[125(4) K]	[36(6) K]	[113(6) K]	[45.1(13) K]	[105(2) K]
	τ_0/s	$1.8(4) \times 10^{-6}$	$2.4(7) \times 10^{-8}$	$5(2) \times 10^{-6}$	$4.2(2) \times 10^{-8}$	$4.9(4) \times 10^{-6}$	$1.0(2) \times 10^{-7}$

exhibit zero-dc-field slow magnetic relaxation in the only slightly extended T-range of 2–18 K (2–15 K for the fitted ac curves) in comparison to **1–3** but with the symmetrical shapes of the $\chi''_M(\nu)$ maxima typical for single relaxation. Moreover, the positions of χ''_M maxima for **1–3** are almost invariant on temperature below 6 K suggesting the strong QTM effect.[75] In **1@Y–3@Y**, they are more dependent on the frequency and shifted toward its lower range below 100 Hz. This indicates that the magnetic dilution leads to at least partial suppression of the QTM which should be related to the cancelling of remaining magnetic interactions between Ho^{III} centres. All these findings were quantified by analysing temperature dependences of the extracted relaxation times in **1–3** and **1@Y–3@Y** (Fig. 2b, and S8–S13†). The $\ln(\tau)$ *versus* T^{-1} plots for all phases strongly deviate from linearity expected for the Arrhenius-type dependence of an Orbach relaxation. Nevertheless, the higher temperature regimes were employed in fitting to the Arrhenius law (Fig. S8–S13†) which results in the effective energy barriers, ΔE lying in the range of 25–40 cm^{-1} (Table 1). These values increase upon magnetic dilution to the range of 73–87 cm^{-1}. However, even for **1@Y–3@Y**, the $\ln(\tau)$ *versus* T^{-1} dependences still deviate from linearity suggesting the presence of the QTM and other relaxation processes such as the Raman relaxation in all investigated compounds. Therefore, the reliable discussion on the SMM effect in **1–3** and **1@Y–3@Y** needs the fitting of the whole $\ln(\tau)$ *versus* T^{-1} curves taking into account three accessible magnetic relaxation processes. It was performed using eqn (1):

$$\tau^{-1} = \tau_0^{-1} \exp\left(\frac{-\Delta E}{k_B T}\right) + \tau_{QTM}^{-1} + C_{Raman} T^n \qquad (1)$$

where the first term represents a T-activated Orbach process depicted by the ΔE energy barrier and the attempt time, τ_0, the second term shows the QTM effect, while the last one reflects the Raman relaxation with the C_{Raman} parameter and the n parameter ranging from *ca.* 2 to 9. As a result, five free variables must be taken into account for the fitting of relaxation times which gave the difficult issue of overparameterization. It was solved using the ΔE values of an Orbach process obtained in the *ab initio* calculations (see below) which were, then, fixed in the fitting procedure. The identical energy barriers were used for **1** and its diluted sample of **1@Y** as they contain the analogous Ho^{III}–Co^{III} molecules with the expected identical Ho^{III} crystal field effect. The same assumption was done for the other pairs of **2** and **2@Y** as well as **3** and **3@Y**. This approach resulted in the high-quality fits and the consistent best-fit parameters gathered in Table 1. Searching for even more reliable determination of parameters for Orbach, Raman, and QTM relaxation processes, we also performed the ac magnetic measurements under variable dc fields for magnetically diluted samples (Fig. S14–S20, Table S5†). The dc magnetic field partially reduces the QTM effect leading to the longer magnetic relaxation. This effect works only in the low dc field regime resulting in the small optimal dc fields of 150 Oe and 100 Oe for **1@Y** and **2@Y–3@Y**, respectively. For higher dc fields, the relaxation becomes faster which can be ascribed to the appearance of a field-induced direct process. Moreover, even for optimal dc fields, the QTM relaxation rate is non-negligible and has to be taken into account for a reliable fitting. Thus, to deal with the issue of overparameterization, we performed the simultaneous fitting of the temperature dependences of relaxation times for both zero and optimal dc fields following eqn (1) with two QTM parameters dependent on the dc field (Fig. S20 and Table S5†). Even using such an approach, it was not possible to reliably determine the energy barriers (ΔE) of Orbach relaxation as the obtained ΔE values of high experimental errors are significantly overestimated when confronted with the results of the *ab initio* calculations (see below). Therefore, also for the simultaneous fitting for zero and optimal dc fields for **1@Y–3@Y**, the fixed ΔE values taken from the *ab initio* calculations were employed to produce the final best-fit parameters (Table 1 and S5†).

The best-fit parameters representing the ac magnetic data confirm the presence of three different relaxation processes (Orbach, Raman, and QTM) in **1–3** and **1@Y–3@Y**. The best-fit curves with the visualized contribution from the QTM are presented in Fig. 2b while an insight into all relaxation pathways is

shown in Fig. S8–S13, S15, S17, and S19–S20.† The obtained parameters prove the SMM character of **1–3** and show that the highest single-ion anisotropy represented by the highest energy barrier of an Orbach process of 89.8 cm^{-1} (129.2 K) is observed in **1**, the slightly smaller ΔE of 86.7 cm^{-1} (124.8 K) in **2**, and a much smaller value of 78.7 cm^{-1} (113.2 K) in **3**. However, the strength of the QTM adopts a different trend as the slowest related relaxation time, τ_{QTM} is observed in **3**, much faster in **1**, and the strongest QTM in **2**. The Raman relaxation also differs within **1–3**. **1** and **3** show very similar contributions from this relaxation which is depicted by nearly identical, *ca.* T^{-3} dependence of the related relaxation time, τ_{Raman}, while **2** exhibits the weaker thermal variation of τ_{Raman}, close to T^{-2}. It indicates the important role of a diamagnetic metal ion in the modification of Raman relaxation of attached paramagnetic Ho^{III} centres which can be ascribed to the modulated phonon modes scheme going from Ho–Co (**1**) and Ho–Ir (**3**) to Ho–Rh (**2**) crystal lattices.[81,82] In this regard, the critical role can be played partially by the distinguishable energies of numerous available vibrational states (Fig. S1†) as well as by the water content which is slightly different for the Rh^{III} analogue (see Experimental details). The results for **1@Y–3@Y** indicate that the magnetic dilution affects both the QTM and Raman relaxation pathways. The magnetic dilution leads to the stronger temperature dependence of the Raman relaxation time as depicted by the increase of the power "*n*" from 3.04, 1.90, and 3.09, to 3.95, 2.57, and 3.77, for **1@Y**, **2@Y**, and **3@Y**, respectively. This can be explained by the modification of a phonon mode scheme upon the replacement of paramagnetic and heavier Ho^{III} centres with diamagnetic and much lighter Y^{III} centres. As the magnetic dilution is similar within the whole series of **1@Y–3@Y**, the resulting changes in the Raman relaxation process were also found to be analogous. The magnetic dilution leads also to the partial suppression of the QTM as depicted by the significant slowdown of the τ_{QTM} which is in line with the shift of the $\chi''_M(\nu)$ maxima to lower frequencies (Fig. 2a). The most efficient weakening of the QTM is observed in **2**, while smaller QTM changes are ascribed to **1** and **3** (Fig. 2b). The final τ_{QTM} value is the highest (5.8 ms) in **3@Y** which means that the slowest magnetic relaxation is achievable for Ho^{III}–Ir^{III} molecules.

To rationalize the differences in the experimental SMM characteristics in **1–3**, the *ab initio* calculations of the Ho^{III} crystal-field effect were performed (Fig. 3, and S21–S23, Tables S6–S10†). The calculations were of a CASSCF/RASSI/SINGLE_ANISO type executed within an OpenMolcas package using the experimental geometries of {Ho[$M(CN)_6$]} molecules from the SC-XRD analysis (Fig. S21, details in the ESI†).[83] In the first approach, the dinuclear molecules of **1–3** were used for the calculations. For each case, three basis sets (small, S model; large, L model; and very large, V model) differing in the applied basis function qualities for the selected parts of calculated structural fragments were employed (Table S6†). All of them reveal the whole energy splitting of the ground $^5I_8$ multiplet of *ca.* 300 cm^{-1} in **1–3** (Tables S7–S9†). As Ho^{3+} is a non-Kramers ion, it is necessary to separately consider each of the 16 m_J levels of the ground multiplet as the degeneracy of 8 possible m_J doublets is not ensured.[53–64] However, in all applied basis sets,

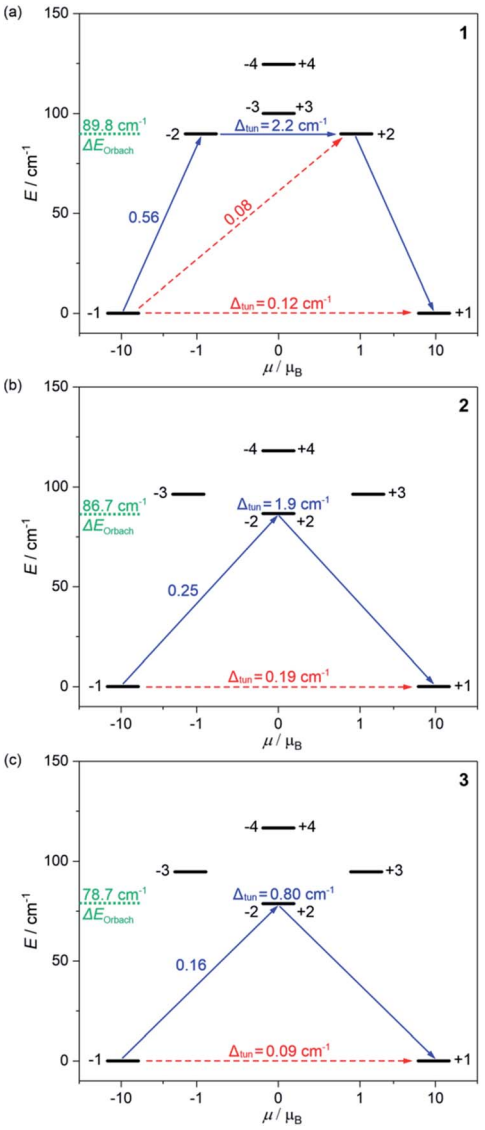

Fig. 3 The energy splitting of the ground $^5I_8$ multiplet of Ho^{III} in **1** (a), **2** (b), and **3** (c) obtained from the *ab initio* calculations. Only the lowest energy part was presented. The resulting energy barriers of the Orbach relaxation were shown in green colour. The numbers above each arrow represent the corresponding matrix element of the transversal magnetic moment while the Δ_{tun} shows the tunnelling gap of the indicated doublets. Red arrows indicate the less possible whereas blue arrows show the most probable relaxation pathway. The scheme is obtained for the L–W models (Table S8†).

the pairs of the lowest lying m_J levels of **1–3** are close in energy, and well-separated from other states lying at least 70 cm^{-1} higher. These ground states are of a predominant $|\pm 8\rangle$ character (*ca.* 97%) with the high value of the g_z component (>19.5) of their pseudo-*g*-tensors, as expected for the Ho^{III} SMMs of the pseudo-D_{5h} symmetry,[61] but there are the non-negligible admixtures of others states, mainly *ca.* 2% of $|\pm 5\rangle$. It results in the non-zero energy difference between the two lowest lying states (Tables S7–S9†). This tunneling gap (Δ_{tun}) directly affects the QTM strength, and should completely vanish in the QTM-free SMMs. The Δ_{tun} values in **1–3** are relatively high, lying in

the range of 0.16–0.34 cm^{-1}, which should lead to the fast QTM rather cancelling the zero-dc-field SMM effect.[53–64] This is in contrast to the experimental observation of slow magnetic relaxation in **1–3** under $H_{dc} = 0$ (Fig. 2); thus, we re-considered the performed *ab initio* calculations. Firstly, we found that the increase of the size of the basis sets from the S to L models leads to the decrease in the Δ_{tun} values, *e.g.* from 0.26 to 0.18 cm^{-1} in **1** (Tables S7–S8†). However, the change in the very large basis sets did not follow this trend as the V model slightly overestimates the whole energy splitting (Table S9†). Thus, we expanded the calculated structural fragments by taking into account crystallization water (W models, Fig. S21†), and we repeated the *ab initio* calculations for all basis sets. The resulting S–W, L–W and V–W models gave the further decrease of the Δ_{tun} values to 0.12, 0.19, and 0.09 for **1**, **2**, and **3**, respectively, for the L–W models (Table S8†). This indicates a crucial role of the second coordination sphere for the Ho^{III} crystal-field effect in **1–3**. For **3**, in the L–W model showing the lowest Δ_{tun}, we also performed the calculations with the enlarged active space using a RASSCF scheme but the Δ_{tun} value remained similar (Table S10†). Due to the lowest Δ_{tun} values, we used the results of the L–W models for further discussion. They well reproduce the experiment (Fig. S7†), both the $\chi_M T(T)$ and $M(H)$ plots, however, the similar magnetic curves were simulated with the other models (Fig. S22†).

The energy splitting scheme of the ground $^5I_8$ multiplet of Ho^{III} in **1–3** for the lowest energy region is shown in Fig. 3. The smallest tunnelling gap, Δ_{tun} is observed in **3**, the slightly higher in **1**, and the highest in **2**, which is in good agreement with the acceleration of the QTM relaxation time, τ_{QTM} in the trend of **3**, **1**, and **2** (Table 1). As the magnetically diluted **1@Y–3@Y** better represent the intrinsic QTM of Ho^{III} complexes, we investigated the related values of τ_{QTM}^{-1} in the function of the square of the Δ_{tun} (Fig. S23†). A linear dependence suggests that the experimental QTM changes in **1–3** are exclusively due to the variable Δ_{tun} related to the composition of the ground states (Table S8†). While the Δ_{tun} values between the lowest lying pairs of m_J levels are small, the analogous tunnelling gaps for higher lying sublevels are much higher, at least 0.8 cm^{-1} for the whole series of **1–3**. This proves that an Orbach relaxation occurs through the first excited m_J states (blue arrows in Fig. 3). Thus, the average energy positions of these m_J states represent the energy barriers of an Orbach process, ΔE. The *ab initio* studies reveal the highest ΔE of 89.8 cm^{-1} in **1**, a lower of 86.7 cm^{-1} in **2**, and the lowest of 78.7 cm^{-1} in **3**. The validity of this trend was proved using the ΔE values in the successful fitting of the *T*-dependences of relaxation times (see above).

The results of *ab initio* calculations well rationalize the observed differences in the SMM effects of **1–3**. However, the obtained Δ_{tun} values between the ground m_J sublevels remain at the level of 0.09–0.19 cm^{-1} for the optimal L–W models (Fig. 3).[53–64] Moreover, we investigated the ac magnetism for the series of variously diluted $\{Ho_xY_{1-x}[Co^{III}(CN)_6]\}$ (x = 0.03, 0.05, 0.08, 0.16, 0.22, and 0.33; **1@Y-Ho$_x$Y$_{1-x}$Co**) systems. We found a strong correlation between the relaxation time and the amount of Ho^{III} centres which can be assigned to the gradual weakening of the QTM effect (Fig. S24†). In particular, the above-mentioned **1@Y** (x = 0.11) was shown to contain the remaining QTM effect as **1@Y-Ho$_{0.03}$Y$_{0.97}$Co** reveals a nearly two times slower relaxation time. This indicates that ideally isolated Ho^{III} complexes of **1–3** exhibit an almost fully quenched QTM effect which is not perfectly reflected in the results of *ab initio* studies. It may be related to the non-ideal crystallographic data, *e.g.* the imperfect findings of the hydrogen positions.[83] However, the final explanation of the observed zero-dc-field SMM effects in **1–3** is related to the additional energy splitting occurring by taking into account the hyperfine interactions of magnetic moment of electrons with the nuclear spin of Ho^{III} (I = 7/2 for ^{165}Ho isotope of 100% abundance).[53,61,84–87] We performed the field-dependent ac magnetic studies for **1@Y–3@Y** revealing the characteristic oscillations of relaxation times under the increasing dc field which is the sign of hyperfine interaction (Fig. S25–S28†).[61] Then, using the crystal field parameters from the *ab initio* calculations, we determined the energy splitting due to the hyperfine interactions (Tables S11–S15, details in the ESI†). The hyperfine parameter, A_{hf} of 0.025 cm^{-1} was optimized by comparison with the field-variable ac magnetic data on the basis of the Zeeman effect and the avoided level crossing rule (Fig. S28†). As a result, instead of one ground quasi-doublet, we obtained 8 ground hyperfine Kramer doublets, and all appeared to be very axial with the very small values of transversal g_x and g_y components (<0.0045) in the whole series of **1–3** (Table S15†). This indicates the efficient suppression of the QTM effect in all compounds. However, the residual non-zero transversal components of the *g*-tensors remain, which stays in line with the observation of a non-negligible QTM relaxation rate even for the magnetically diluted samples of **1@Y–3@Y** under the optimal dc field (Fig. S14–S19†). As a result, a magnetic hysteresis loop is not detectable even at the lowest accessible temperature of 1.8 K which is typical among the reported Ho^{III} SMMs.[53–64] In **1–3**, this effect can be ascribed to the insufficiently pure $m_J = \pm 8$ ground state which is related to the non-ideal D_{5h} geometry of Ho^{III} complexes (Fig. 1). All differences within **1–3**, including the strength of the residual QTM and in the energy barriers found the rational reflection in the energy splitting modified by the hyperfine interactions (see discussion in the ESI†).

The distinguishable SMM features of **1–3** can be ascribed to the subtle structural variation (Table S3†). The Ho^{III} complexes reveal a pentagonal bipyramidal geometry, thus, the important role in the magnitude of energy splitting, determining the ΔE, can be played by the distances from Ho1 to the axial O2 atoms of 4-pyridone bearing a partial negative charge (Fig. 2b). They are similar in **1–3** but the increasing trend in the Ho1–O2 bond lengths of 2.231, 2.233, and 2.235 Å for **1**, **2**, and **3**, corresponds well to the decreasing ΔE from **1** to **3**. The negative charge is also ascribed to the O1 atoms lying in the equatorial plane. Their distances to Ho1 also follow the increasing trend of 2.272, 2.276, and 2.278 Å for **1**, **2**, and **3**, respectively. Moreover, their positions within the plane, represented by the O2–Ho1–O1 angles, are more deviated from the 90° in **1** (2.72°) and **2** (2.69°) than in **3** (2.37°). All these differences contribute to the stronger crystal field in **1–2**. In contrast, the distance between Ho1 and the N1 atom of cyanido bridge is shorter in **2** (2.434 Å) than in **1**

(2.460 Å) and **3** (2.452 Å). The shorter distance of the cyanido ligand to Ho1 in the Ho–Rh species can lead to the stronger mixing of the m_J levels giving the stronger QTM. Moreover, the average distance between Ho1 and equatorial atoms is longer in **1** and **3** (2.356 Å) than in **2** (2.346 Å) which may delimit their disturbing role in the stabilization of the $|\pm 8\rangle$ ground state in **1** and **3** producing the lower QTM rate. These findings prove a non-innocent role of $[M^{III}(CN)_6]^{3-}$ ions in modulating the Ho^{III} SMM effect.

Optical thermometry

Due to the presence of multiple emissive components of Ho^{III}, 4-pyridone, and $[M^{III}(CN)_6]^{3-}$ ions,[65,78,88] optical properties of **1–3** and their Y^{III}-diluted analogues, including **1@Y–3@Y**, were investigated (Fig. 4, 5, S29–S33, and Tables 3, S16–S17†). Solid-state UV-vis-NIR absorption spectra (Fig. S29†) indicate that **1–3** exhibit a strong UV absorption band at 270 nm accompanied with weaker sharp peaks in the visible region (Fig. S29†). The UV absorption can be mainly assigned to the spin-allowed π–π* electronic transitions of 4-pyridone. In **1** and **2**, the d–d $^1A_{1g} \rightarrow {}^1T_{2g}$ transitions of $[M^{III}(CN)_6]^{3-}$ ions also contribute to the UV absorption when another $^1A_{1g} \rightarrow {}^1T_{1g}$ transition results in the weaker band at *ca.* 310 nm, well distinguished only in **1**.[79] In **3**, the 4-pyridone transitions completely dominate as the absorption of the $[Ir^{III}(CN)_6]^{3-}$ ion is shifted below 250 nm.[88] In contrast, the weak absorption peaks covering the whole visible range can be exclusively assigned to f–f electronic transitions of Ho^{III} centres occurring thanks to their ladder-type electronic structure (Table S16†).[89] Following the strong UV and weak visible light absorption, the possible photoluminescence of **1–3** was examined. We checked various excitation wavelengths from the UV range but no distinct emission signal was observed. Only under the UV excitation around 370 nm, corresponding to the typical excitation of 4-pyridone phosphorescence of the π–π* origin,[79] weak ligand-based emission was detected (Fig. S30†). This can be assigned to the strong luminescence quenching, including the re-absorption effect related to Ho^{III} complexes, present in large numbers in **1–3**. This is supported by the presence of a series of negative re-absorption peaks occurring within the broad emission band. Moreover, we detected strong room-temperature blue emission originating from 4-pyridone for **4**, containing exclusively $\{Y^{III}[Co^{III}(CN)_6]\}$ molecules (Fig. S30†). Therefore, two trimetallic derivatives with the variable Ho : Y ratio, **1@Y** (**1@Y-$Ho_{0.11}Y_{0.97}Co$**) and **1@Y-$Ho_{0.33}Y_{0.67}Co$**, were examined, and distinct ligand emission with a series of negative Ho^{III}-based re-absorption peaks was observed. The overall emission is weakened while the relative intensity of the negative peaks increases with the increasing amount of Ho^{III}. We found that **1@Y** exhibits a good equilibrium giving the significant ligand emission and easily detectable sharp re-absorption peaks. Therefore, for this compound and for their Rh- and Ir-based analogues, **2@Y** and **3@Y**, we performed detailed luminescence studies (Fig. 4 and S31–S33†).

All Y^{III}-diluted compounds, regardless of UV excitation, **1@Y–3@Y** reveal similar ligand-based emission at 300 K, and no other emission peaks, possibly originating from $[M^{III}(CN)_6]^{3-}$ electronic states,[88] were detected. However, the emission maxima slightly vary from 420 nm in **3@Y**, 435 nm in **1@Y**, to 445 nm in **2@Y** (Fig. S31–S33†). Taking **1@Y** as an example, we found that, under the optimal 370 nm excitation, a series of Ho^{III}-re-absorption-based negative peaks are observed within the 4-pyridone emission pattern (Fig. 4a). By comparison with the interpreted UV-vis absorption spectra (Table S16†), these peaks were assigned to the Ho^{III} f–f electronic transitions from the ground $^5I_8$ multiplet to various excited states. Upon cooling of **1@Y** to 10 K, a gradual increase of overall emission intensity was detected; however, the re-absorption effect also intensified

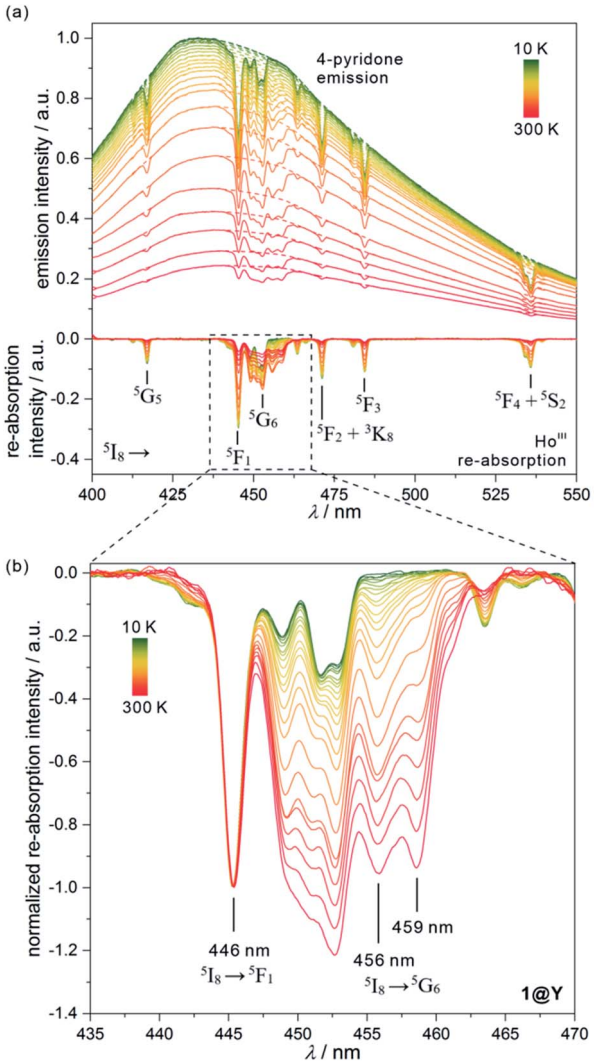

Fig. 4 Temperature-dependent emission spectra of **1@Y** measured under 370 nm light irradiation along with the extracted luminescence re-absorption spectra obtained after the subtraction of the ligand emission component (a), with the enlargement of the re-absorption spectra in the range of 435–470 nm showing the strongest thermometric effect (b). In (a), top part, the dashed lines represent the simulated shape of each ligand emission band, while in the bottom part, the assignment of main re-absorption peaks to the electronic transitions of Ho^{III} was shown. The spectra in (b) were normalized to the re-absorption peak at 446 nm. The indicated peaks at 446, 456, and 459 nm were used in the thermometric parameters.

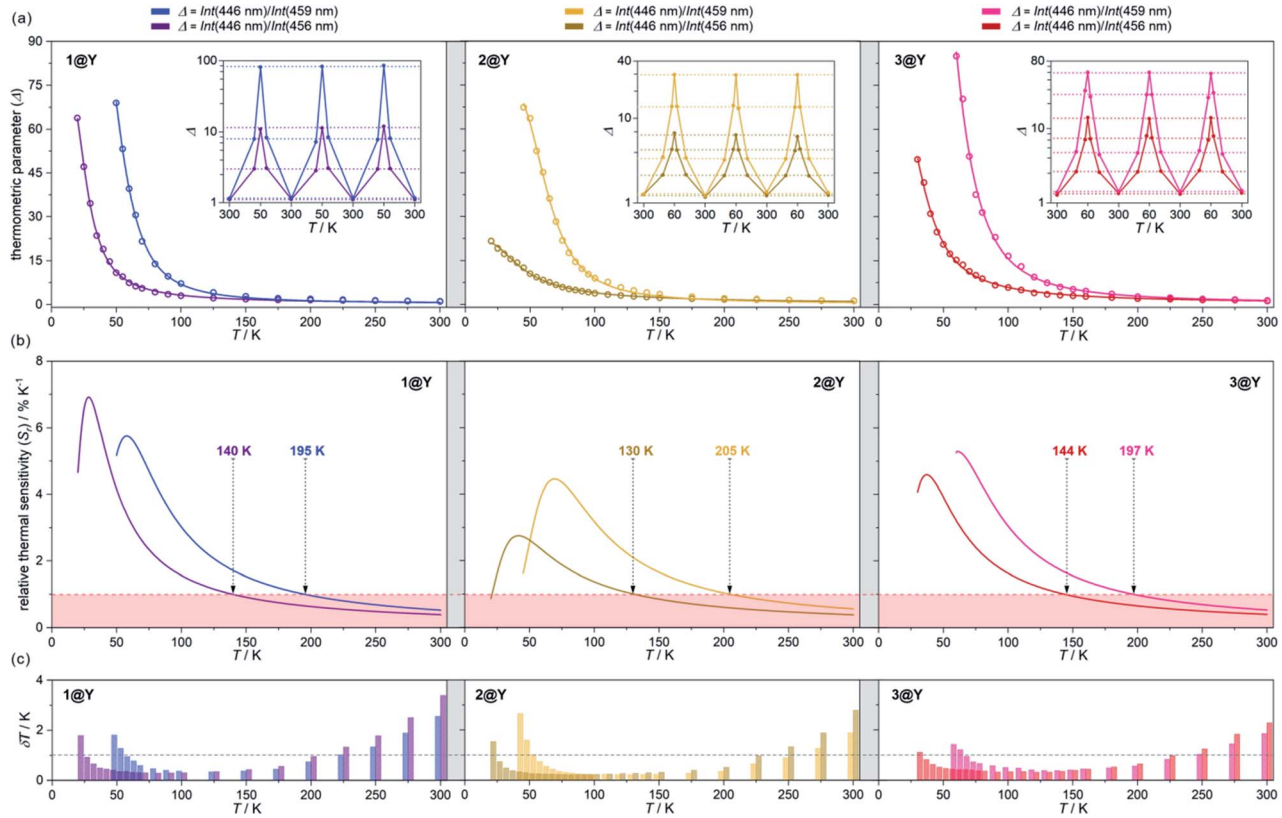

Fig. 5 Luminescent thermometric characteristics of **1@Y** (left), **2@Y** (centre), and **3@Y** (right) using two selected ratiometric parameters, Δ, obtained from the temperature-dependent emission spectra (Fig. 4 and S31–S33†): the experimental temperature dependences of Δ (empty circles) together with the fitted calibration curves (eqn (2), solid lines) and the repeatability of thermometric behaviour within three cooling–heating cycles in the insets (a), the temperature dependences of relative thermal sensitivity, S_r calculated from calibration curves (solid lines) with the indicated regime below 1% K^{-1} (coloured area) and the indicated temperature below which S_r exceeds 1% K^{-1} (b), and the temperature uncertainties, δT at each measurement point with the indicated limit of $\delta T < 1$ K (dashed line) (c).

as visible in the deeper negative peaks. More importantly, we observed distinguishable changes in the strength of re-absorption peaks at different wavelengths which is a prerequisite for optical thermometry. To quantify this effect, the re-absorption peaks were extracted from the featureless ligand emission bands used as a background (Fig. 4a). The strongest re-absorption effect accompanied by the most significant thermally induced changes was detected in the 435–470 nm range related to the combined contributions from the $^5I_8 \rightarrow {}^5F_1$ and $^5I_8 \rightarrow {}^5G_6$ electronic transitions. We analysed this region by applying the intensity normalization to the distinct peak at 446 nm of the $^5I_8 \rightarrow {}^5F_1$ transition (Fig. 4b). As a result, we detected a strong temperature dependence of the neighbouring re-absorption peaks whose relative intensity decreases upon cooling. Primarily, this can be explained by their different origin, that is the assignment to the $^5I_8 \rightarrow {}^5G_6$ transition, which is expected to show distinguishable thermal variation.[70,71] Considering all accessible peaks from this pattern, we found the strongest thermal changes for peaks at 456 and 459 nm. They almost disappear at low temperatures suggesting that they can be connected with the hot bands from one of the excited m_J levels of the ground $^5I_8$ multiplet (Fig. 3). Thus, their strong T-dependence in relation to the peak at 446 nm is a combined result of the appearance of hot bands and variable thermal dependences of different electronic transitions. The analogous T-dependences of luminescence spectra and the extracted re-absorption effect were found for **2@Y** and **3@Y**, thus, they were analysed in an identical manner (Fig. S31–S33†).

To perform a precise characterization of the thermometric effect and discuss the differences along the series of **1@Y–3@Y**, two different thermometric parameters (Δ) were defined as the ratios between the intensities of transitions located at 446 nm and two selected bands at 456 and 459 nm (Fig. 4b). These thermometric parameters strongly depend on temperature, particularly in the 25–200 K range (Fig. 5a). They correspond to the thermal variation of absorption peaks which can be mainly assigned to the role of thermally activated vibrational motions governing the intensity of the f–f electronic transitions.[70,71,90,91] Within this model, applying for T-dependent absorption spectra of Ho^{III}-based systems,[70,71] the Δ values of **1@Y–3@Y** can be presented using eqn (2):

$$\Delta = \Delta_0 \Big/ \left[\coth\left(\frac{\Delta E_v}{2T}\right) + C\right] \qquad (2)$$

where Δ_0 is the uncorrected thermometric parameter at $T = 0$ K, ΔE_v is the activation energy for the critical effective vibration,

and C is the empirical correction constant which allows to determine the corrected thermometric parameter for $T = 0$ K, $\Delta_{0,\mathrm{corr}} = \Delta_0/(1 + C)$. In principle, one should consider the separate temperature dependences of both absorption peaks with two distinguishable ΔE_v values. However, in the discussed re-absorption spectra, the first peak at 446 nm, was used for the intensity normalization, thus, the [coth ($\Delta E_v/2T$) + C] contribution represents the differential thermal variation between two applied peaks. Using eqn (2), the experimental T-dependences of thermometric parameters for **1@Y–3@Y** were successfully fitted, resulting in the thermometric calibration curves (Fig. 5a and Table S17†). In all compounds, the ΔE_v values were higher for the 459 nm line (300–350 K) than for the 456 nm peak (100–130 K) which are directly related to the ranges of the strongest $\Delta(T)$-dependences, lying in the 60–120 K and 20–80 K regions, respectively. More precise discussion was enabled by plotting of the relative thermal sensitivity, $S_r(T)$ curves, obtained using the calibration curves and the relation of $S_r = (\partial\Delta/\partial T)/\Delta$ (Fig. 5b), and, further by plotting of the related temperature uncertainty, $\delta T(T)$ dependences, using the relation of $\delta T = (\delta\Delta/\Delta)/S_r$ where $\delta\Delta/\Delta$ is the relative error in the determination of the thermometric parameter (Fig. 5c).[35,92]

The current arbitrary conditions for good optical thermometers are defined as the temperature regions for which $S_r > 1\%$ K^{-1} along with $\delta T < 1$ K, and these boundaries were depicted in Fig. 5b and c. It is clearly seen that reliable optical thermometric behaviour was achieved in **1@Y–3@Y** for the broad ranges from *ca.* 20 K up to 200 K. In all compounds, this region is adjusted by the selection of the re-absorption peak. The 459 nm band is more appropriate for the temperatures above 60 K but works up to even 200 K whereas the 459 nm line serves reliably from very low temperatures of 20 K but only to the limits of *ca.* 140 K. The operating ranges of optical thermometers are also modulated by the selection of cyanido complexes within the series of **1@Y–3@Y** (Table 2). The broadest range, covering 150 K, accompanied by the highest temperature of good performance thermometry of 205 K, was achieved in **2@Y** for the Δ parameter involving the 459 nm peak. This is due to the flattened calibration curve with the relatively small changes but extended within the large T-region (Fig. 5a). However, this leads to the lower values of S_r for **2@Y** as depicted by the comparison of maximal thermal sensitivities within the series (Table 2). The highest S_r of 6.9% K^{-1} is accessible for **1@Y** which is the impressive value among the optical thermometers.[35–39] Slightly lower maximal S_r limits are observed in **3@Y** while **2@Y** exhibits significantly lower thermal sensitivities, never exceeding 4.5% K^{-1}. All these findings indicate a non-negligible role of hexacyanidometallates in controlling of the optical thermometer performance. This is an indirect influence as the applied thermometric effect utilizes the intrinsic absorption property of Ho^{III} and phosphorescence of the organic ligand. Moreover, the procedure for extracting the re-absorption effect (Fig. 4) made the resulting optical thermometer basically independent of the overall emission intensity which is significantly amended by the cyanido complexes exhibiting the electronic states at the variable parts of the visible range.[88] However, the thermally tunable absorption properties of Ho^{III} centres can be also affected by the cyanido complexes due to the role of their rich vibrational states such as cyanido stretching vibrations appearing in the 2100–2200 cm^{-1} region of the IR spectrum (Fig. S1†). The energies of these states decrease in the trend of **2** > **3** > **1**,[88] corresponding well to the observed improvement of the maximal thermal sensitivity (Table 2). It can be suggested that one of the vibrational modes contributing to the thermal variation of the Ho^{III} electronic states belong to the coordinated cyanido ligand, and their energy, depending on the transition metal, plays a non-innocent role. This is in line with the recent findings on the critical role of cyanido stretching vibrations in the $[M(CN)_x]$-dependent tuning of optical properties of f-block metal complexes.[88,93] In addition to the above characterization of optical thermometry, we have also performed three thermal heating–cooling cycling experiments checking the thermometric parameters at three different temperatures (Fig. 5a). It demonstrates the perfect repeatability (>97%) of the thermometric behaviour in the whole series of **1@Y–3@Y**.

The representative region of 435–470 nm of the luminescence re-absorption spectra of **1@Y–3@Y** (Fig. 4 and S31–S33†), which shows the most effective thermometric effect, can be also used for magneto–optical correlations. This part of the spectrum contains the complex pattern related mainly to the $^5I_8 \rightarrow {}^5G_6$ electronic transitions, only partially overlapped with the bands assignable to the $^5I_8 \rightarrow {}^5F_1$ transition. The analysis of the low-temperature (10 K) spectrum in this range provides the information regarding only the energy splitting of the excited $^5G_6$ multiplet while the higher-temperature patterns become the complex sum of electronic transitions from various states of

Table 2 Comparison of luminescent thermometric performance of **1@Y**, **2@Y**, and **3@Y** for two different thermometric parameters, Δ. The notation *Int*(λ) stands for the intensity of the luminescence re-absorption effect at the indicated wavelength (Fig. 4). The bold values represent the best parameters in the context of the good thermometric performance range (the temperature region for which $S_r > 1\%$ K^{-1} and $\delta T < 1$ K), and in the context of the highest achievable maximal thermal sensitivity, S_r

Compound	Thermometric parameter, Δ	Good thermometric performance range	Maximal S_r value (at temperature, T)
1@Y	*Int*(446 nm)/*Int*(456 nm)	25–140 K (115 K range)	**6.9% K^{-1} ($T = 28$ K)**
	Int(446 nm)/*Int*(459 nm)	60–195 K(135 K)	5.8% K^{-1} ($T = 58$ K)
2@Y	*Int*(446 nm)/*Int*(456 nm)	25–130 K (105 K)	2.7% K^{-1} ($T = 42$ K)
	Int(446 nm)/*Int*(459 nm)	**55–205 K (150 K)**	4.5% K^{-1} ($T = 69$ K)
3@Y	*Int*(446 nm)/*Int*(456 nm)	35–144 K (109 K)	4.6% K^{-1} ($T = 37$ K)
	Int(446 nm)/*Int*(459 nm)	70–197 K (127 K)	5.3% K^{-1} ($T = 61$ K)

the ground $^5I_8$ multiplet not only to the lowest state of the $^5G_6$ multiplet but also to the higher-lying ones (Fig. S34†). This hampers a straightforward optical estimation of the anisotropic energy barrier (ΔE) of Orbach relaxation which is illustrated by the energy difference between the two lowest quasi-doublets of the ground multiplet (Fig. 3).[19–27] However, the comparison of the low- (10 K) and high-temperature (300 K) re-absorption patterns agrees well with the calculated energy splitting of the ground multiplet determined from the *ab initio* calculations, including both the energy positions of the maxima related to the groups of closely lying excited states as well as the overall energy of the crystal field splitting for the ground multiplet, slightly exceeding 300 cm^{-1} (Fig. S34, and detailed discussion in the ESI†). Therefore, the luminescence re-absorption spectra support the results of *ab initio* calculations (Fig. 3, and Table S8†), thus supporting also the interpretation of magnetic relaxation effects in **1–3**.

Conclusions

We report a series of dinuclear cyanido-bridged molecules, $\{[Ho^{III}(4\text{-pyridone})_4(H_2O)_2][M^{III}(CN)_6]\}$ (M = Co, Rh, and Ir) together with their magnetically Y^{III}-diluted analogues exhibiting a Single-Molecule Magnet (SMM) character thanks to the combined contributions from the pentagonal bipyramidal geometry, the axial charge distribution, and the supporting role of the hyperfine interactions. They realize a novel concept of SMM-based optical thermometers exploring a temperature-dependent luminescence re-absorption effect of Ho^{III} centres detectable within the emission of organic ligands. We prove that the application of Ho^{III} complexes is a promising tool for achieving both the slow magnetic relaxation effect and the highly sensitive optical thermometry. Our approach is different from the reported strategies towards magnetic optical thermometers as we explore the re-absorption effect of Ho^{III} and commonly observed ligand-based emission. It opens a convenient route to generate the optical thermometric effect by the incorporation of Ho^{III} centres into diverse emissive organic or inorganic matrices. This idea can be also developed in the smart SMM-based opto-magnetic devices built of Ho^{III} magnetic molecules deposited onto the emissive surfaces. Therefore, we show a promising avenue to combine the SMM property with optical thermometry without the necessity to control luminescence quenching effects within the lanthanide complex. Moreover, we achieved high thermal sensitivity, reaching up to 6.9% K^{-1} at the lowest temperatures below 40 K which is the working range of SMMs, thus, such molecular systems are good candidates for SMM-based devices with self-monitoring of temperature. Our approach takes advantage of the supporting hexacyanidometallates of transition metals which were able to modulate the SMM features and the optical thermometric performance. The best-performance SMM, in the context of the most efficient suppression of the QTM, was obtained using heavy $[Ir^{III}(CN)_6]^{3-}$ ions, which have never before been applied for the construction of molecular nanomagnets. Their utility in the further improvement of Ho^{III}-based SMMs will be now investigated along with testing of diverse emissive ligands and coordination skeletons cooperating with Ho^{III} centres in the generation of multifunctional opto-magnetic materials.

Conflicts of interest

There are no conflicts to declare.

Acknowledgements

This work was financed by the National Science Centre of Poland within the OPUS-15 project, Grant no. 2018/29/B/ST5/00337, and by the Japanese Society for the Promotion of Sciences (JSPS) within the Grant-in-Aid for JSPS fellows (grant no. 19J22088) and the Grant-in-Aid for Scientific Research on Innovative Area Soft Crystals (area no. 2903, 17H06367). M. Z. acknowledges the research grant under the "Diamond Grant" program (DI2018 017948) of the Polish Ministry of Science and Higher Education. The present research was also supported in part by a JSPS Grant-in-Aid for Specially Promoted Research Grant No. 15H05697, Grant-in-Aid for Scientific Research(A) Grant No. 20H00369, KAKENHI Grant No. 19K05366, and IM-LED LIA (CNRS). We acknowledge the Cryogenic Research Centre, The Univ. of Tokyo, the Centre for Nano Lithography & Analysis, The Univ. of Tokyo supported by MEXT, and Quantum Leap Flagship Program (Q-LEAP) by MEXT.

Notes and references

1 J. Ferrando-Soria, H. Khajavi, P. Serra-Crespo, J. Gascon, F. Kapteijn, M. Julve, F. Lloret, J. Pasan, C. Ruiz-Perez, Y. Journaux and E. Pardo, *Adv. Mater.*, 2012, **24**, 5625–5629.
2 C. R. Gros, M. K. Peprah, B. D. Hosterman, T. V. Brinzari, P. A. Quintero, M. Sendova, M. W. Meisel and D. R. Talham, *J. Am. Chem. Soc.*, 2014, **136**, 9846–9849.
3 S. Ohkoshi, S. Takano, K. Imoto, M. Yoshikiyo, A. Namai and H. Tokoro, *Nat. Photonics*, 2014, **8**, 65–71.
4 S. Chorazy, K. Nakabayashi, S. Ohkoshi and B. Sieklucka, *Chem. Mater.*, 2014, **26**, 4072–4075.
5 M. Estrader, J. S. Uber, L. A. Barrios, J. Garcia, P. Lloyd-Williams, O. Roubeau, S. J. Teat and G. Aromi, *Angew. Chem., Int. Ed.*, 2017, **56**, 15622–15627.
6 A. C. Felts, A. Slimani, J. M. Cain, M. J. Andrus, A. R. Ahir, K. A. Abboud, M. W. Meisel, K. Boukheddaden and D. R. Talham, *J. Am. Chem. Soc.*, 2018, **140**, 5814–5824.
7 C. Lochenie, K. Schötz, F. Panzer, H. Kurz, B. Maier, F. Puchtler, S. Agarwal, A. Köhler and B. Weber, *J. Am. Chem. Soc.*, 2018, **140**, 700–709.
8 B. Benaicha, J. Van Do, A. Yangui, N. Pittala, A. Lusson, M. Sy, G. Bouchez, H. Fourati, C. J. Gomez-Garcia, S. Triki and K. Boukheddaden, *Chem. Sci.*, 2019, **10**, 6791–6798.
9 N. Ishikawa, M. Sugita, T. Ishikawa, S. Koshihara and Y. Kaizu, *J. Am. Chem. Soc.*, 2003, **125**, 8694–8695.
10 J. M. Zazdrozny, D. J. Xiao, M. Atanasov, G. J. Long, F. Grandjean, F. Neese and J. R. Long, *Nat. Chem.*, 2013, **5**, 577–581.

11 M. Mannini, F. Pineider, P. Sainctavit, C. Danieli, E. Otero, E. Sciancelepore, A. M. Talarico, M.-A. Arrio, A. Cornia, D. Gatteschi and R. Sessoli, *Nat. Mater.*, 2009, **8**, 194–197.
12 M. Mannini, F. Bertani, C. Tudisco, L. Malavolti, L. Poggini, K. Misztal, D. Menozzi, A. Motta, E. Otero, P. Ohresser, P. Sainctavit, G. G. Condorelli, E. Dalcanale and R. Sessoli, *Nat. Commun.*, 2014, **5**, 4582.
13 A. Candini, S. Klyatskaya, M. Ruben, W. Wernsdorfer and M. Affronte, *Nano Lett.*, 2011, **11**, 2634–2639.
14 S. Thiele, F. Balestro, R. Ballou, S. Klyatskaya, M. Ruben and W. Wernsdorfer, *Science*, 2014, **344**, 1135–1138.
15 J. D. Rinehart and J. R. Long, *Chem. Sci.*, 2011, **2**, 2078–2085.
16 J.-H. Jia, Q.-W. Li, Y.-C. Chen, J.-L. Liu and M.-L. Tong, *Coord. Chem. Rev.*, 2019, **378**, 365–381.
17 C. A. P. Goodwin, F. Ortu, D. Reta, N. Chilton and D. P. Mills, *Nature*, 2017, **548**, 439–442.
18 F.-S. Guo, B. M. Day, Y.-C. Chen, M.-L. Tong, A. Mansikkamäki and R. A. Layfield, *Science*, 2018, **362**, 1400–1403.
19 F. Pointillart, B. Le Guennic, S. Golhen, O. Cador, O. Maury and L. Ouahab, *Chem. Commun.*, 2013, **49**, 615–617.
20 Q.-W. Li, J.-L. Liu, J.-H. Jia, Y.-C. Chen, J. Liu, L.-F. Wang and M.-L. Tong, *Chem. Commun.*, 2015, **51**, 10291–10294.
21 K. Soussi, J. Jung, F. Pointillart, B. Le Guennic, B. Lefeuvre, S. Golhen, O. Cador, Y. Guyot, O. Maury and L. Ouahab, *Inorg. Chem. Front.*, 2015, **2**, 1105–1117.
22 F. Pointillart, B. Le Guennic, O. Cador, O. Maury and L. Ouahab, *Acc. Chem. Res.*, 2015, **48**, 2834–2842.
23 E. L. Gavey, M. Al Hareri, J. Regier, L. D. Carlos, R. A. S. Ferreira, F. S. Razavi, J. M. Rawson and M. Pilkington, *J. Mater. Chem. C*, 2015, **3**, 7738–7747.
24 S. Chorazy, M. Rams, K. Nakabayashi, B. Sieklucka and S. Ohkoshi, *Chem.–Eur. J.*, 2016, **22**, 7371–7375.
25 Y.-C. Chen, J.-L. Liu, Y. Lan, Z.-Q. Zhong, A. Mansikkamäki, L. Ungur, Q.-W. Li, J.-H. Jia, L. F. Chibotaru, J.-B. Han, W. Wernsdorfer, X.-M. Chen and M.-L. Tong, *Chem.–Eur. J.*, 2017, **23**, 5708–5715.
26 M. A. Sorensen, U. B. Hansen, M. Perfetti, K. S. Pedersen, E. Bartolome, G. S. Simeoni, H. Mutka, S. Rols, M. Jeong, I. Zivkovic, M. Retuerto, A. Arauzo, J. Bartolome, S. Pilgkos, H. Weihe, L. H. Doerrer, J. van Slageren, H. M. Ronnow, K. Lefmann and J. Bendix, *Nat. Commun.*, 2018, **9**, 1292.
27 J. J. Zakrzewski, S. Chorazy, K. Nakabayashi, S. Ohkoshi and B. Sieklucka, *Chem.–Eur. J.*, 2019, **25**, 11820–11825.
28 Y. Bi, C. Chen, Y.-F. Zhao, Y.-Q. Zhang, S.-D. Jiang, B.-W. Wang, J.-B. Han, J.-L. Sun, Z.-Q. Bian, Z.-M. Wang and S. Gao, *Chem. Sci.*, 2016, **7**, 5020–5031.
29 D. Errulat, R. Marin, D. A. Galico, K. L. M. Harriman, A. Pialat, B. Gabidullin, F. Iikawa, O. D. D. Couto Jr, J. O. Moilanen, E. Hemmer, F. A. Sigoli and M. Murugesu, *ACS Cent. Sci.*, 2019, **5**, 1187–1198.
30 K. Kumar, D. Abe, K. Komori-Orisaku, O. Stefanczyk, K. Nakabayashi, J. R. Shakirova, S. P. Tunik and S. Ohkoshi, *RSC Adv.*, 2019, **9**, 23444–23449.
31 G. Brunet, R. Marin, M.-J. Monk, U. Resch-Genger, D. A. Galico, F. A. Sigoli, E. A. Suturina, E. Hemmer and M. Murugesu, *Chem. Sci.*, 2019, **10**, 6799–6808.
32 D. A. Galico, R. Marin, G. Brunet, D. Errulat, E. Hemmer, F. A. Sigoli, J. O. Moilanen and M. Murugesu, *Chem.–Eur. J.*, 2019, **25**, 14625–14637.
33 J. Wang, J. J. Zakrzewski, M. Heczko, M. Zychowicz, K. Nakagawa, K. Nakabayashi, B. Sieklucka, S. Chorazy and S. Ohkoshi, *J. Am. Chem. Soc.*, 2020, **142**, 3970–3979.
34 M. Fondo, J. Corredoira-Vazquez, A. M. Garcia-Deibe, J. Sanmartin-Matalobos, M. Amoza, A. M. P. Botas, R. A. S. Ferreira, L. D. Carlos and E. Colacio, *Inorg. Chem. Front.*, 2020, **7**, 3019–3029.
35 J. Rocha, C. D. S. Brites and L. D. Carlos, *Chem.–Eur. J.*, 2016, **22**, 14782–14795.
36 Y. Hasegawa and Y. Kitagawa, *J. Mater. Chem. C*, 2019, **7**, 7494–7511.
37 M. Hatanaka, Y. Hirai, Y. Kitagawa, T. Nakanishi, Y. Hasegawa and K. Morokuma, *Chem. Sci.*, 2017, **8**, 423–429.
38 D.-F. Lu, Z.-F. Hong, J. Xie, X.-J. Kong, L.-S. Long and L.-S. Zheng, *Inorg. Chem.*, 2017, **56**, 12186–12192.
39 G. Bao, K.-L. Wong, D. Jin and P. A. Tanner, *Light: Sci. Appl.*, 2018, **7**, 96.
40 C. D. S. Brites, M. C. Fuertes, P. C. Angelome, E. D. Martinez, P. P. Lima, G. J. A. A. Soler-Illia and L. D. Carlos, *Nano Lett.*, 2017, **17**, 4746–4752.
41 X. Zhu, J. Li, X. Qiu, W. Feng and F. Li, *Nat. Commun.*, 2018, **9**, 2176.
42 R. G. Geitenbeek, A.-E. Nieuwelink, T. S. Jacobs, B. B. V. Salzmann, J. Goetze, A. Meijerink and B. M. Weckhuysen, *ACS Catal.*, 2018, **8**, 2397–2401.
43 C. D. S. Brites, S. Balabhadra and L. D. Carlos, *Adv. Opt. Mater.*, 2018, 18012139.
44 M. Atzori, L. Tesi, E. Morra, M. Chiesa, L. Sorace and R. Sessoli, *J. Am. Chem. Soc.*, 2016, **138**, 2154–2157.
45 J. Liu, Y.-C. Chen, J.-L. Liu, V. Vieru, L. Ungur, J.-H. Jia, L. F. Chibotaru, Y. Lan, W. Wernsdorfer, S. Gao, X.-M. Chen and M.-L. Tong, *J. Am. Chem. Soc.*, 2016, **138**, 5441–5450.
46 G. Zucchi, O. Maury, P. Thuery, F. Gumy, J.-C. G. Bünzli and M. Ephritikhine, *Chem.–Eur. J.*, 2009, **15**, 9686–9696.
47 T. Xia, Y. Cui, Y. Yang and G. Qian, *J. Mater. Chem. C*, 2017, **6**, 5044–5047.
48 I. Hernandez, Y.-X. Zheng, M. Motevalli, R. H. C. Tan, W. P. Gillin and P. B. Wyatt, *Chem. Commun.*, 2013, **49**, 1933–1935.
49 S. Chorazy, M. Rams, J. Wang, B. Sieklucka and S. Ohkoshi, *Dalton Trans.*, 2017, **47**, 13668–13672.
50 L. Marciniak and A. Bednarkiewicz, *Sens. Actuators, B*, 2017, **243**, 388–393.
51 K. S. Pedersen, J. Dreiser, H. Weihe, R. Sibille, H. V. Johannesen, M. A. Sorensen, B. E. Nielsen, M. Sigrist, H. Mutka, S. Rols, J. Bendix and S. Piligkos, *Inorg. Chem.*, 2015, **54**, 7600–7606.
52 T.-Q. Liu, P.-F. Yan, F. Luan, Y.-X. Li, J.-W. Sun, C. Chen, F. Yang, H. Chen, X.-Y. Ziu and G. M. Li, *Inorg. Chem.*, 2015, **54**, 221–228.
53 N. Ishikawa, M. Sugita and W. Wernsdorfer, *J. Am. Chem. Soc.*, 2005, **127**, 3650–3651.

54 M. A. AlDamen, S. Cardona-Serra, J. M. Clemente-Juan, E. Coronado, A. Gaita-Arino, C. Marti-Gastaldo, F. Luis and O. Montero, *Inorg. Chem.*, 2009, **48**, 3467–3479.
55 R. J. Blagg, F. Tuna, E. J. L. McInnes and R. E. P. Winpenny, *Chem. Commun.*, 2011, **47**, 10587–10589.
56 S. Ghosh, S. Datta, L. Friend, S. Cardona-Serra, A. Gaita-Arino, E. Coronado and S. Hill, *Dalton Trans.*, 2012, **41**, 13697–13704.
57 S. Cardono-Serra, J. M. Clemente-Juan, E. Coronado, A. Gaita-Arino, A. Camon, M. Evangelisti, F. Luis, M. Martinez-Perez and J. Sese, *J. Am. Chem. Soc.*, 2012, **134**, 14982–14990.
58 J. Dreiser, R. Westerström, Y. Zhang, A. A. Popov, L. Dunsch, K. Krämer, S.-X. Liu, S. Decurtins and T. Greber, *Chem.–Eur. J.*, 2014, **20**, 13536–13540.
59 M. Viciano-Chumillas, F. Koprowiak, I. Mutikainen, W. Wernsdorfer, T. Mallah and H. Bolvin, *Phys. Rev. B*, 2017, **96**(8), 214427.
60 F. Pointillart, O. Cador, B. Le Guennic and L. Ouahab, *Coord. Chem. Rev.*, 2017, **346**, 150–175.
61 Y.-C. Chen, J.-L. Liu, W. Wernsdorfer, D. Liu, L. F. Chibotaru, X.-M. Chen and M.-L. Tong, *Angew. Chem., Int. Ed.*, 2017, **56**, 4996–5000.
62 T. P. Latendresse, V. Vieru, A. Upadhyay, N. S. Bhuvanesh, L. F. Chibotaru and M. Nippe, *Chem. Sci.*, 2020, **11**, 3936–3951.
63 Y. Ma, Y.-Q. Zhai, Y.-S. Ding, T. Han and Y.-Z. Zheng, *Chem. Commun.*, 2020, **56**, 3979–3982.
64 S.-M. Chen, Y.-Q. Zhang, J. Xiong, B.-W. Wang and S. Gao, *Inorg. Chem.*, 2020, **59**, 5835–5844.
65 E. G. Moore, G. Szigethy, J. Xu, L.-O. Pälsson, A. Beeby and K. M. Raymond, *Angew. Chem., Int. Ed.*, 2008, **47**, 9500–9503.
66 S. Chorazy, M. Arczynski, K. Nakabayashi, B. Sieklucka and S. Ohkoshi, *Inorg. Chem.*, 2015, **54**, 4724–4736.
67 M. K. Muhata, T. Koppe, K. Kumar, H. Hofsäss and U. Vetter, *Sci. Rep.*, 2020, **10**, 8775.
68 J.-C. Rybak, L. V. Meyer, J. Wagenhöfer, G. Sextl and K. Müller-Buschbaum, *Inorg. Chem.*, 2012, **51**, 13204–13213.
69 T. Ribbeck, S. H. Zottnick, C. Kerpen, J. Landmann, N. V. Ignat'ev, K. Müller-Buschbaum and M. Finze, *Inorg. Chem.*, 2017, **56**, 2278–2286.
70 S. Gutzov, S. Berendts, M. Lerch, C. Geffert, A. Börger and K. D. Becker, *Phys. Chem. Chem. Phys.*, 2009, **11**, 636–640.
71 V. Petrov, N. Danchova and S. Gutzov, *Spectrochim. Acta, Part A*, 2020, **227**, 117527.
72 T. Shiraki, A. Dawn, Y. Tsuchiya and S. Shinkai, *J. Am. Chem. Soc.*, 2010, **132**, 13929–13935.
73 C. D. S. Brites, P. P. Lima, N. J. O. Silva, A. Millan, V. S. Amaral, F. Palacio and L. D. Carlos, *Nanoscale*, 2012, **4**, 4799–4829.
74 K. Kumar, S. Chorazy, K. Nakabayashi, H. Sato, B. Sieklucka and S. Ohkoshi, *J. Mater. Chem. C*, 2018, **6**, 8372–8384.
75 Y. Xin, J. Wang, M. Zychowicz, J. J. Zakrzewski, K. Nakabayashi, B. Sieklucka, S. Chorazy and S. Ohkoshi, *J. Am. Chem. Soc.*, 2019, **141**, 18211–18220.
76 S. Chorazy, J. J. Zakrzewski, M. Reczyński, K. Nakabayashi, S. Ohkoshi and B. Sieklucka, *J. Mater. Chem. C*, 2019, **7**, 4164–4172.
77 Y. Liu, Y.-C. Chen, J. Liu, W.-B. Chen, G.-Z. Huang, S.-G. Wu, J. Wang, J.-L. Liu and M.-L. Tong, *Inorg. Chem.*, 2020, **59**, 687–694.
78 S. Chorazy, J. Wang and S. Ohkoshi, *Chem. Commun.*, 2016, **52**, 10795–10798.
79 J. Wang, S. Chorazy, K. Nakabayashi, B. Sieklucka and S. Ohkoshi, *J. Mater. Chem. C*, 2018, **6**, 473–481.
80 F. Habib, P.-H. Lin, J. Long, I. Korobkov, W. Wernsdorfer and M. Murugesu, *J. Am. Chem. Soc.*, 2011, **133**, 8830–8833.
81 L. Spree, C. Schlesier, A. Kostanyan, R. Westerström, T. Greber, B. Büchner, S. M. Avdashenko and A. A. Popov, *Chem.–Eur. J.*, 2020, **26**, 2436–2449.
82 L. Anh Ho and L. F. Chibotaru, *Phys. Rev. B*, 2018, **97**, 024427.
83 L. Ungur and L. F. Chibotaru, *Chem.–Eur. J.*, 2017, **23**, 3708–3718.
84 W. Wernsdorfer, A. Caneschi, R. Sessoli, D. Gatteschi, A. Cornia, V. Villar and C. Paulsen, *Phys. Rev. Lett.*, 2000, **84**, 2965–2968.
85 D. Gatteschi and R. Sessoli, *Angew. Chem., Int. Ed.*, 2003, **42**, 268–297.
86 F. Troiani, A. Ghirri, M. Affronte, S. Carretta, P. Santini, G. Amoretti, S. Piligkos, G. Timco and R. E. P. Winpenny, *Phys. Rev. Lett.*, 2005, **94**(4), 207208.
87 N. Ishikawa, M. Sugita and W. Wernsdorfer, *Angew. Chem., Int. Ed.*, 2005, **44**, 2931–2935.
88 S. Chorazy, J. J. Zakrzewski, M. Reczyński and B. Sieklucka, *Chem. Commun.*, 2019, **55**, 3057–3060.
89 J. B. Gruber, G. W. Burdick, U. V. Valiev, K. L. Nash, S. A. Rakhimov and D. K. Sardar, *J. Appl. Phys.*, 2009, **106**, 113110.
90 S. Gutzov, A. Börger and K. D. Becker, *Phys. Chem. Chem. Phys.*, 2007, **9**, 491–496.
91 B. Di Bartolo, *Optical Interactions in Solids*, Wiley, 1968, pp. 20–35.
92 M. Back, E. Trave, J. Ueda and S. Tanabe, *Chem. Mater.*, 2016, **28**, 8347–8356.
93 J. J. Zakrzewski, B. Sieklucka and S. Chorazy, *Inorg. Chem.*, 2020, **59**, 1393–1404.